


# Heterogeneous catalysis from structure to activity via SSW-NN method

Cite as: J. Chem. Phys. **151**, 050901 (2019); <https://doi.org/10.1063/1.5113673>

Submitted: 06 June 2019 . Accepted: 09 July 2019 . Published Online: 05 August 2019

Sicong Ma , Cheng Shang , and Zhi-Pan Liu 

## COLLECTIONS

 This paper was selected as Featured



View Online



Export Citation



CrossMark

## ARTICLES YOU MAY BE INTERESTED IN

### Atomistic structure learning

The Journal of Chemical Physics **151**, 054111 (2019); <https://doi.org/10.1063/1.5108871>

### Physical implications of $so(2, 1)$ symmetry in exact solutions for a self-repressing gene

The Journal of Chemical Physics **151**, 041101 (2019); <https://doi.org/10.1063/1.5105361>

### Perspective: Computational chemistry software and its advancement as illustrated through three grand challenge cases for molecular science

The Journal of Chemical Physics **149**, 180901 (2018); <https://doi.org/10.1063/1.5052551>

The Journal  
of Chemical Physics

Submit Today

The Emerging Investigators Special Collection and Awards  
Recognizing the excellent work of early career researchers!



# Heterogeneous catalysis from structure to activity via SSW-NN method

Cite as: *J. Chem. Phys.* **151**, 050901 (2019); doi: [10.1063/1.5113673](https://doi.org/10.1063/1.5113673)

Submitted: 6 June 2019 • Accepted: 9 July 2019 •

Published Online: 5 August 2019



View Online



Export Citation



CrossMark

Sicong Ma,  Cheng Shang,<sup>a)</sup>  and Zhi-Pan Liu<sup>a)</sup> 

## AFFILIATIONS

Collaborative Innovation Center of Chemistry for Energy Material, Shanghai Key Laboratory of Molecular Catalysis and Innovative Materials, Key Laboratory of Computational Physical Science, Department of Chemistry, Fudan University, Shanghai 200433, China

<sup>a)</sup>Electronic addresses: [cshang@fudan.edu.cn](mailto:cshang@fudan.edu.cn) and [zpliu@fudan.edu.cn](mailto:zpliu@fudan.edu.cn)

## ABSTRACT

Modern research on heterogeneous catalysis calls for new techniques and methods to resolve the active site structure and reaction intermediates at the atomic scale. Here, we overview our recent progress on large-scale atomistic simulation via potential energy surface (PES) global optimization based on neural network (NN) potential, focusing on methodology details and recent applications on catalysis. The combination of stochastic surface walking (SSW) global optimization and the NN method provides a convenient and automated way to generate the transferable and robust NN potential for global PES, which can be utilized to reveal new chemistry from the unknown region of PES with an affordable computational cost. The predictive power of SSW-NN is demonstrated in several examples, where the method is applied to explore the material crystal phases, to follow the surface structure evolution under high pressure hydrogen and to determine the ternary oxide phase diagram. The limitations and future directions to develop the SSW-NN method are also discussed.

© 2019 Author(s). All article content, except where otherwise noted, is licensed under a Creative Commons Attribution (CC BY) license (<http://creativecommons.org/licenses/by/4.0/>). <https://doi.org/10.1063/1.5113673>

## I. INTRODUCTION

Heterogeneous catalysts are renowned for their great complexity of material composition and surface structures. There has been a long history for both experiment and theory in the struggle to resolve the active site of catalysts that are responsible for activity and selectivity.<sup>1–4</sup> The latest progress in experiments are represented by high spatial resolution techniques, e.g., the spherical aberration-corrected high-resolution transmission electron microscope, and synchrotron-based measurements, e.g., extended X-ray absorption fine structure. On the other hand, as a direct tool to correlate the atomic structure with its energy, theoretical simulations have been widely practiced in modeling catalyst structures and even predicting the activity, especially with the advent of density functional theory (DFT) calculations.<sup>5</sup> However, DFT simulation is generally limited to hundreds of atoms and thus fails to explore exhaustively the phase space of complex catalysts, such as amorphous structures, multicomponent oxide/alloys.<sup>6–8</sup>

To identify the active site of catalysts from theory, it is essential to explore the potential energy surface (PES) of exposed surfaces.

This requires not only a fast and reliable approach to evaluate the energetics of structures but also an efficient method to explore the structural phase space. As for PES calculation methods, most are based on quantum mechanics as represented by DFT calculations, while the empirical force field calculations and more recently an artificial neural network (NN)<sup>9</sup> potential method (Fig. 1), despite their limitation in transferability, are also often utilized in material applications. Since catalytic conversion involves the chemical bond making and breaking, DFT calculations have been the most popular way to provide an accurate description of reactions with reasonable computational cost. The computation speed of DFT is sensitive to the complexity of the employed density-functional (e.g., PBE<sup>10</sup> and HSE06<sup>11</sup>) and has a poor scaling [at least  $O(N \ln N)$ ]. It is very difficult to explore the reaction network in large catalytic systems (e.g., >100 atoms). As a promising alternative, the NN potential method developed in the past decade demonstrates its power in treating complex PES problems, from the gas phase reactions to material dynamics.<sup>12–15</sup> Recently, it was also utilized for solving the structures of heterogeneous catalysts, for example, Pd(O),<sup>16</sup> Pt(H),<sup>17</sup> CuAu,<sup>18,19</sup> CuCeO,<sup>20</sup> and CuZnO.<sup>21</sup> Unlike the traditional force field

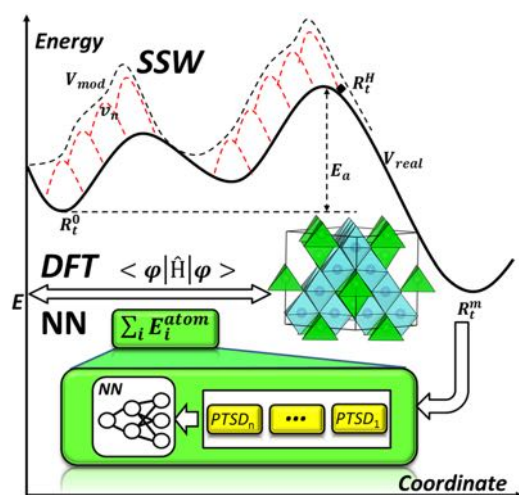


**FIG. 1.** Scheme of the SSW-NN. The total energy can be obtained from the NN potential, which replaces the high cost procedure to solve the Schrödinger equation. The total energy of a system in the NN potential is a sum over all atomic energy. The atomic energy involves power-type structural descriptor (PTSD) computation (see Sec. II C 2) and a NN evaluation. The SSW global optimization is utilized to explore the PES and produce new structures.

potentials, the NN potential is able to describe chemical reactions with high accuracy as long as the training dataset contains the reactive data, such as the transition state (TS).

In parallel to the progress in PES evaluation methods, many PES exploration methods have been developed through the past decades. As catalytic reactions and the structural reconstruction occur generally above ambient temperatures involving high barrier processes, traditional molecular dynamic (MD) simulation is often not appropriate for active site identification. Instead, the global optimization methods, which can overcome the high barrier on PES, are desirable. The common global optimization methods include simulated annealing,<sup>22</sup> genetic algorithm,<sup>23</sup> basin hopping,<sup>24</sup> and stochastic surface walking (SSW).<sup>25,26</sup>

This perspective serves to outline our recent contributions in methodology development toward catalyst PES exploration and active site identification. We will show that the combination of the global NN potential with the SSW method, SSW-NN, provides a powerful platform to resolve the catalyst structure which can finally lead to the prediction of catalyst activity from first principles. The SSW-NN method together with other common atomic simulation techniques is now implemented in LASP software, *Large-scale Atomic Simulation with neural network Potential*, which allows one, within a user-friendly platform, to perform first principles calculations, NN potential generation, and atomic simulation using the NN potential.<sup>27</sup>

## II. SSW-NN METHOD

### A. SSW method

The SSW algorithm<sup>25</sup> is an unbiased global optimization method that can explore both minima and saddle points on PES.

SSW implements an automated climbing mechanism to manipulate a structural configuration moving smoothly from a local minimum to a high-energy configuration along one random mode direction. The method was initially developed for aperiodic systems,<sup>26</sup> such as molecules and clusters, and has been extended to periodic crystals.<sup>28</sup>

The SSW method inherits the idea of bias-potential driven constrained-Broyden-dimer (BP-CBD) method for TS location. In one particular SSW step, labeled as  $t$ , a modified PES  $V_{mod}$ , as shown in Eq. (1) and Fig. 1, is utilized for moving from the current minimum,  $R_t^0$ , to a high energy configuration,  $R_t^H$  (the climbing), in which a series of bias Gaussian potential  $v_n$  ( $n$  is the index of the bias potential,  $n = 1, 2, \dots, H$ ) is added one by one consecutively along the direction  $N_t^H$  (Fig. 1),

$$V_{mod} = V_{real} + \sum_{n=1}^{NG} v_n \\ = V_{real} + \sum_{n=1}^{NG} w_n * \exp[-((R_t - R_t^n) \cdot N_t^n)^2 / (2 \times ds^2)], \quad (1)$$

where  $R_t$  is the coordination vector of the structure and  $V_{real}$  represents the unmodified PES;  $R_t^n$  is the  $n$ -th local minima along the movement trajectory on the modified PES that is created after adding  $n$  Gaussian functions. The Gaussian function is controlled by its height  $w$  and its width  $ds$  and is always added along one particular walking direction as defined by  $N_t^n$ . Once the  $R_t^H$  is reached, all bias potential are removed and local optimization is performed to quench the structure to a new minimum. Different from the BP-CBD method, each SSW step (from one minimum to another) will choose a random direction to perturb the structure after the direction is refined (softened) using the biased-CBD method. At the end of the SSW step, a structure selection module, e.g., in the Metropolis Monte Carlo scheme, is applied to accept/refuse the new minimum.

### B. High-dimensional NN architecture

The artificial NN method was first developed to understand the signal processing in the brain.<sup>29</sup> In the following decades, NN evolves into a class of powerful algorithms applied to a variety of fields from numerical prediction, pattern recognition to data classification. It is most renowned for the powerful ability to establish the functional relationship between independent variables and target (dependent) values via nonlinear “black box” data processing.

In 2007, Behler and Parrinello implemented the high-dimensional NN (HDNN) architecture for material simulation, which trains the first principles PES dataset to generate NN potential.<sup>30–32</sup> In the approach, the total energy  $E_{tot}$  of system is written as the summation over all atoms [Eq. (2)] (see Fig. 1). Each atom is represented by a standard feed-forward (FFNN), where the input layer is a series of structural descriptors to describe the atom bonding environment and the output layer yields the atomic energy  $E_i$  ( $i$  indexes atoms),

$$E_{tot} = \sum_i E_i(\mathbf{R}). \quad (2)$$

The structural descriptors can, in principle, be any functional forms of atomic coordinates.<sup>33–35</sup> In their original work, Behler *et al.* suggests a series of rotation-invariant symmetry functions as the

structural descriptors, which are Gaussian type functions of intrinsic coordinates (pair distance, angles).<sup>30</sup> The NN potential can be trained by minimizing the cost function that measures the deviation of the NN output with respect to the training set properties, e.g., total energy, force, and stress.<sup>36,37</sup> The training set is a large structure dataset on PES with accurate energetics and forces, most often computed from first principles calculations. More details on HDNN can be found in previous reviews.<sup>35,38,39</sup>

## C. SSW-NN

### 1. Self-learning procedure

Unlike classical force field potentials, the NN potential is generally found to have a limited predictability beyond the training dataset, presumably due to the numerical function fitting by a large number of parameters. The key to improve the quality of the NN potential therefore relies much on the representativity of the PES dataset. To overcome this deficiency of the NN potential, we propose in 2017 a global-to-global scheme to generate the global NN (G-NN) potential for material simulation.<sup>37</sup> This scheme combines the SSW global optimization for data generation, the HDNN for PES description, and a self-learning procedure<sup>17</sup> to expand the dataset and upgrade the NN potential, the so-called SSW-NN method. The self-learning procedure of SSW-NN is described briefly as follows (see Fig. 2).

**The first stage** constructs an initial dataset by performing in parallel short-time SSW sampling based on first-principles DFT calculations. These DFT calculations are often restricted to small systems (typically below 20 atoms) and with a low accuracy calculation setup to speed up the global PES sampling. After the PES data are obtained from SSW, a small dataset is randomly selected and computed using DFT with a high accuracy calculation setup. This stage produces a dataset with the most common atomic environment for the target PES.

**The second stage** generates a NN potential using the current first principles dataset. The key features of our NN potential will be detailed in Subsection II C 2.

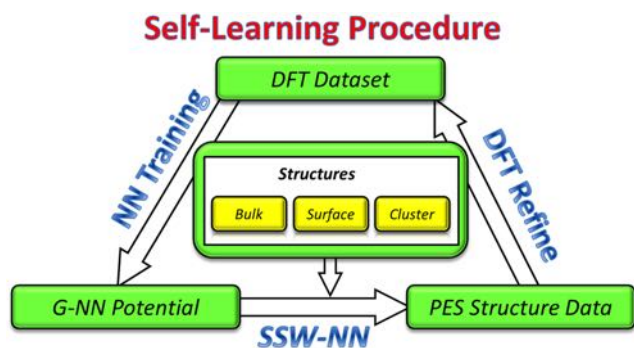


**FIG. 2.** Self-learning procedure of the global NN potential. The global dataset is first generated using high accuracy DFT calculations, which is then trained to obtain the global NN potential (G-NN). Then, an additional dataset is generated by SSW sampling based on the G-NN potential. This additional dataset is then fed back into the global dataset and a new cycle self-learning starts.

**The third stage** expands the dataset by carrying out long-time SSW global PES sampling using the current NN potential. These SSW-NN simulations start from a variety of initial structures with different morphology, including bulk, surface, and clusters, different chemical compositions, and different number of atoms per unit cell. A small additional dataset is thus obtained from the SSW sampling trajectories, containing the structures on PES either randomly selected or exhibiting new atomic environment (e.g., out-of-bounds in structural descriptor, unrealistic energy/force/curvature). After calculating these additional data by DFT, they are added into the training dataset and the whole self-learning procedure returns back to the previous stage.

Typically, after ~100 iterations, a robust and accurate NN potential can be obtained with a compact training set that contains the most representative structures. We emphasize that it is better to adopt consistent and high accuracy calculation setups in constructing the training dataset using first principles calculations, which can benefit greatly the data transferability and compatibility between systems and also help us to reduce the NN fitting error.

### 2. G-NN potential

Our G-NN potential utilizes our recently proposed power-type structural descriptors (PTSDs)<sup>37</sup> to distinguish different structures on PES. The general forms of the PTSD are described in the following equations:<sup>37</sup>

$$f_c(r_{ij}) = \begin{cases} 0.5 \times \tanh^3 \left[ 1 - \frac{r_{ij}}{r_c} \right], & \text{for } r_{ij} \leq r_c, \\ 0 & \text{for } r_{ij} > r_c \end{cases}, \quad (3)$$

$$R^n(r_{ij}) = r_{ij}^n \cdot f_c(r_{ij}), \quad (4)$$

$$S_i^1 = \sum_{j \neq i} R^n(r_{ij}), \quad (5)$$

$$S_i^2 = \left[ \sum_{m=-L}^L \left| \sum_{j \neq i} R^n(r_{ij}) Y_{Lm}(\mathbf{r}_{ij}) \right|^2 \right]^{\frac{1}{2}}, \quad (6)$$

$$S_i^3 = 2^{1-\zeta} \sum_{j,k \neq i} (1 + \lambda \cos \theta_{ijk})^\zeta \cdot R^n(r_{ij}) \cdot R^m(r_{ik}) \cdot R^p(r_{jk}), \quad (7)$$

$$S_i^4 = 2^{1-\zeta} \sum_{j,k \neq i} (1 + \lambda \cos \theta_{ijk})^\zeta \cdot R^n(r_{ij}) \cdot R^m(r_{ik}), \quad (8)$$

$$S_i^5 = \left[ \sum_{m=-L}^L \left| \sum_{j,k \neq i} R^n(r_{ij}) \cdot R^m(r_{ik}) \cdot R^p(r_{jk}) \cdot (Y_{Lm}(\mathbf{r}_{ij}) + Y_{Lm}(\mathbf{r}_{ik})) \right|^2 \right]^{\frac{1}{2}}, \quad (9)$$

$$S_i^6 = 2^{1-\zeta} \sum_{j,k,l \neq i} (1 + \lambda \cos \delta_{ijkl})^\zeta \cdot R^n(r_{ij}) R^m(r_{ik}) R^p(r_{il}), \quad (10)$$

where  $r_{ij}$  is the internuclear distance between atom  $i$  and  $j$ ,  $\theta_{ijk}$  is the angle centered at  $i$  atom with  $j$  and  $k$  being neighbors ( $i$ ,  $j$ , and  $k$  are atom indices). The key ingredients in PTSD are the cut-off function  $f_c$  that decays to zero beyond the  $r_c$  [Eq. (3)], power-type radial function, trigonometric angular functions, and spherical harmonic function.

In PTSD, the  $S^1$  and  $S^2$  are two-body functions, the  $S^3$ ,  $S^4$ , and  $S^5$  are three-body functions, and the  $S^6$  is a four-body function. The replacement of the Gaussian-type structural descriptor which

was proposed by Behler and Parrinello by the PTSD has several advantages: (i) the computational cost in numerical calculations is reduced; (ii) the adjustable parameters are reduced to one ( $n$ ) that simplifies the search for optimal parameters for two-body function; (iii) the power function when combining with the decaying cut-off function can create radial distributions with flexible peak and shape, which fulfills the similar purpose of Gaussian function (see Fig. 3); (iv) the introduction of different powers ( $n$ ,  $m$ , and  $p$ ) in the three-body function can couple conveniently different radial distributions. (v) The introduction of a spherical function greatly improves the description of the angular environment of atoms.

Our G-NN potential typically has two to three hidden layers and 50–120 neurons for each layer, which leads to the number of network parameters (weights and bias in NN) in the range of  $10^4$ – $10^6$ . The optimization of such a large parameter space is achieved via the quasi-Newton Limited-memory Broyden–Fletcher–Goldfarb–Shanno (L-BFGS) method by simultaneously fitting the total energy, force, and stress from first principles that constitutes the cost function  $J_{tot}$  as follows:

$$J_{tot} = J_E + \rho J_F + \tau J_\sigma$$

$$= \frac{1}{2N} (E^{NN} - E^{real})^2 + \frac{\rho}{6N} (F_{k,\alpha}^{NN} - F_{k,\alpha}^{real})^2$$

$$+ \frac{\tau}{18} (\sigma_{\alpha\beta}^{NN} - \sigma_{\alpha\beta}^{real})^2, \quad (11)$$

where  $\rho = 1$ –10 and  $\tau = 0.05$ –0.1. The training procedure is controlled by a number of hyperparameters, such as the relative weight among energy, force, and stress [ $1:\rho:\tau$  in Eq. (11)], network weight initialization method, type of neuron activation function, and training epochs.<sup>40,41</sup> A prototype of these hyperparameters frequently utilized is summarized in Table I. Due to the structural variety of the global PES, the typical accuracy for G-NN is 5–10 meV/atom for

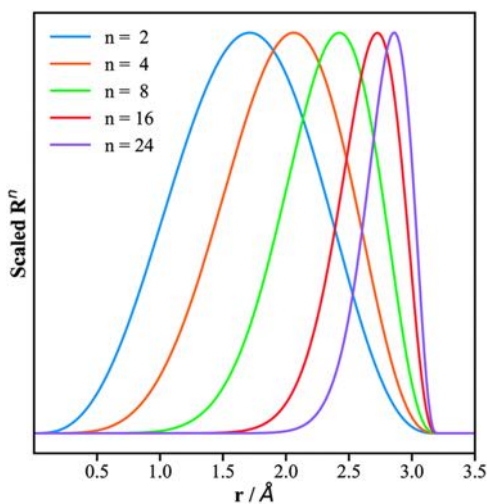


**FIG. 3.** Plots of the radial part of the PTSDs [Eq. (3)] with the same cutoff radius of 3.2 Å but different power  $n$ . The x-axis is the distance  $r$ , while the y-axis is the function value scaled to (0, 1). Reprinted with permission from Huang *et al.*, Chem. Sci. 9(46), 8644–8655 (2018). Copyright 2018 The Royal Society of Chemistry.

**TABLE I.** A prototype of hyperparameters used in our previous works.

Hyper-parameters	Values
Optimization method	L-BFGS
Weight ratio $1:\rho:\tau$	1:5:0.05
Number of hidden layers	2–3
Neuron number in the input layer	100–400
Neuron number in each hidden layer	50–120
Weight initialization method	Xavier initialization
Type of neuron activation function	$\tanh^3$
Size of training data	20 000–100 000
Training epochs	~20 000
Number of weights and bias	$10^4$ – $10^6$

root mean square errors (RMSEs) of energy and 0.1–0.2 eV/Å for RMSE of force.

### III. APPLICATIONS

#### A. PES exploration

The thermodynamics and kinetics of materials are determined by the underlying PES. SSW-NN simulation is such a convenient and efficient tool to establish the global PES for materials. In the past several years, we have mapped out the PESs for a number of systems, e.g., single element crystal (boron),<sup>37</sup> molecular crystal (ice),<sup>42</sup> and metal oxide (TiO<sub>2</sub>, ZnCr<sub>2</sub>O<sub>4</sub>).<sup>43,44</sup> The PESs of TiO<sub>2</sub> and ZnCr<sub>2</sub>O<sub>4</sub> are projected onto a two-dimensional contour map, as shown in Fig. 4, where the structural order parameter (OP) and the relative energy are the x- and y-axis, respectively. The density of the map represented by different colors indicates the density of states (DOS) on PES, showing the energy degeneracy of structural configurations at the same structural OP.

The OP is defined by the following equation:<sup>45</sup>

$$OP_l = \left( \frac{4\pi}{2l+1} \sum_{m=-l}^l \left| \frac{1}{N_{bonds}} \sum_{i \neq j} e^{-\frac{r_{ij}-r_c}{2r_c}} Y_{lm}(\mathbf{n}) \right|^2 \right)^{1/2}, \quad (12)$$

where  $Y_{lm}$  is the spherical harmonic function of degree  $l$  and order  $m$ ;  $\mathbf{n}$  is the normalized direction between all bonded atoms;  $i$  and  $j$  are atoms in the lattice,  $r_{ij}$  is the distance between atom  $i$  and  $j$ , and  $r_c$  is set at 60% of the typical single bond length for  $i$  and  $j$  atoms.  $N_{bonds}$  is the number of bonds. By choosing a suitable degree  $l$ , the order parameter can measure the short- and medium-range ordering of atoms in the lattice and thus distinguish important crystal structures and amorphous structures. For example, it is often straightforward to tell the coordination number from the OP value, e.g., six-coordinated Ti atom with  $OP_2 = 0.3$ –0.5 and five-coordinated Ti atom with  $OP_2 = 0.6$ –0.8 in TiO<sub>2</sub> PES.

As shown in Fig. 4, the PESs of the TiO<sub>2</sub> and ZnCr<sub>2</sub>O<sub>4</sub> shape rather differently: TiO<sub>2</sub> PES like a butterfly while ZnCr<sub>2</sub>O<sub>4</sub> PES like a funnel. At the bottom of the PES, where the low energy structures lie, the TiO<sub>2</sub> PES demonstrates that there are many energetically similar TiO<sub>2</sub> crystal phases but with different structural patterns, having multiple funnels in the butterfly shape. By contrast, ZnCr<sub>2</sub>O<sub>4</sub> PES

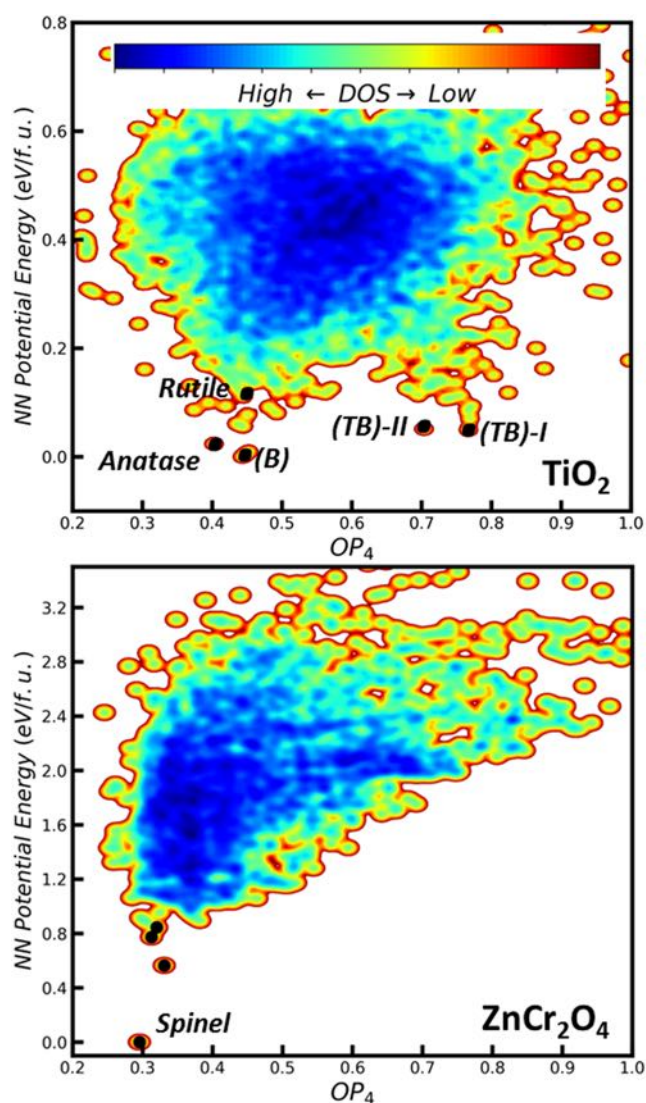


**FIG. 4.** Global PESs of  $\text{TiO}_2$  and  $\text{ZnCr}_2\text{O}_4$  as determined from the SSW-NN global search. The energy (eV/f.u.) of the most stable phase is set as reference zero. The  $x$  axis is the common structure fingerprint for the crystal, namely, the distance-weighted Steinhardt-type order parameter ( $\text{OP}_4$ ) with different angular moment  $L = 2, 4, 6$  which can distinguish different minima, and the  $y$  axis is the relative energy ( $\Delta E$ ) of minima. Reprinted with permission from Ma *et al.*, ACS Appl. Energy Mater. **1**(1), 22–26 (2018). Copyright 2018 American Chemical Society; S. Ma, S.-D. Huang, and Z.-P. Liu, “Dynamic coordination of cations and catalytic selectivity on zinc-chromium oxide alloys during syngas conversion,” Nat. Catal. (published online 2019). Copyright 2019 Nature Publishing Group.

has only a well-defined global minimum, a spineltype structure, and all the other structures are much higher in energy. It is not surprising that more than 10 different  $\text{TiO}_2$  crystal structures have been synthesized in experiment to date [e.g., anatase, rutile, (R), and (H)], while only a spinel phase is known for  $\text{ZnCr}_2\text{O}_4$ .

In addition to the global minimum, the global PES can also reveal unknown metastable structures, which may exhibit

attractive physicochemical properties. In the case of  $\text{TiO}_2$ , it is known in general chemistry that  $[\text{TiO}_6]$  octahedron is the common building block for  $\text{TiO}_2$  crystals. However, a new class of unprecedented microporous  $\text{TiO}_2$  crystalline phases, named  $\text{TiO}_2(\text{TB})$  in Fig. 4, have been identified, which features a special  $[\text{TiO}_5]$  trigonal bipyramidal building block, a large pore size (5–7 Å), and high thermal stability.<sup>43</sup> These microporous materials are predicted to be the candidate of anode materials for Li-ion and Na-ion batteries.<sup>46</sup>

## B. Origin of amorphous $\text{TiO}_x\text{H}_y$ for hydrogen evolution reaction

Black titania ( $\text{TiO}_2$ ) with strong absorption in the entire visible-light spectrum has been found to exhibit the hydrogen evolution reaction (HER) activity several orders higher than the conventional  $\text{TiO}_2$  material.<sup>47–52</sup> Synthesized by hydrogenating pristine  $\text{TiO}_2$ , the as-synthesized black  $\text{TiO}_2$  commonly exhibits a core-shell structure with the amorphous shell, a few nanometers thick, coated on the anatase crystals.<sup>48,53–55</sup> The amorphous shell is believed to provide the catalytic active site and responsible for the enhanced HER activity. However, the structure determination for the amorphous shell is challenging to both experiment and theory, not even mentioning to understand the high HER activity.

To resolve the HER active sites on the amorphous  $\text{TiO}_x\text{H}_y$  shell, we have performed SSW-NN simulation to obtain the  $\text{TiO}_x\text{H}_y$  global dataset with 143 786 structures and built a robust and accurate  $\text{TiO}_x\text{H}_y$  G-NN potential. The structures in the database cover different Ti:O:H ratios, mainly  $\text{Ti}_4\text{O}_7$ ,  $\text{Ti}_4\text{O}_8$ ,  $\text{Ti}_4\text{O}_8\text{H}_x$ ,  $x = 1–4$ ,  $\text{Ti}_8\text{O}_{16}\text{H}_x$ ,  $x = 1–4$  with the bulk, layer, and cluster forms, and also contain large surface systems such as  $\text{Ti}_{56}\text{O}_{112}\text{H}_x$  and molecular systems ( $\text{H}_2$ ,  $\text{H}_2\text{O}$ ). The  $\text{TiO}_x\text{H}_y$  G-NN potential utilizes 201 PTSDs for each element, i.e., 77 two-body PTSDs, 108 three-body PTSDs, and 16 four-body PTSDs, and the network involves two-hidden layers, each with 50 neurons, equivalent to 38 103 network parameters in total. The final RMSEs of energy and force are 9.8 meV/atom and 0.22 eV/Å, respectively.

Using the  $\text{TiO}_x\text{H}_y$  G-NN potential, the thermodynamics phase diagram of  $\text{TiO}_2$  bulk and surface in contact with  $\text{H}_2$  at different temperatures and pressures can thus be determined quantitatively. We found that among common anatase surfaces, only the ridged anatase (112) surface can reconstruct significantly by surface H atoms and a local high H coverage, 0.69 ML, can gradually be built up during the surface amorphization. The amorphous surface exposes different Ti cations, 25% four-coordinated  $\text{Ti}_{4c}$ , 50% five-coordinated  $\text{Ti}_{5c}$ , and 25% six-coordinated  $\text{Ti}_{6c}$  atoms [Fig. 5(a)]. Consistently, the Ti-O bond length has a wide distribution, from 1.8 to 2.2 Å, as compared to 1.9–2.1 Å on a perfect  $\text{TiO}_2$  surface. This high H coverage not only renders the black color of the amorphous  $\text{TiO}_2$  but also provides a low energy reaction channel for HER: a transient Ti-H hydride becomes likely to form on the exposed Ti atoms of the amorphous surface. The nascent TiH hydride can react facily with the neighboring OH to produce  $\text{H}_2$ , where the barrier is more than 1 eV lower than the traditional H coupling channel via two surface OH groups (barrier > 1.9 eV), as shown in Fig. 5(b).<sup>44,56</sup>

We note that after the theoretical work is published, a recent experimental work reveals the presence of TiH hydride on amor-

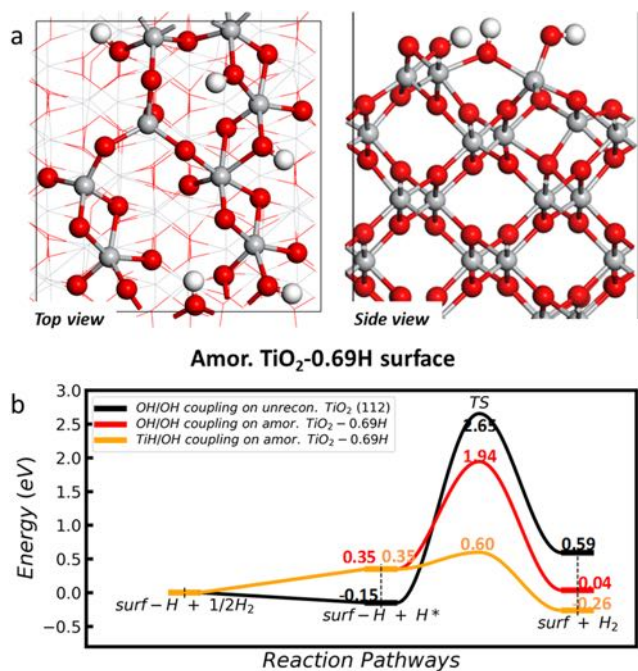


**FIG. 5.** (a) The structure of amorphous  $\text{TiO}_2$  surface with H coverage of 0.69 ML. Ti: gray balls; O: red balls; H: white balls (H in reaction: green ball). (b) The energetic profiles of H coupling via the OH/OH coupling and the TiH/OH coupling mechanisms on the pristine (112) surface and amorphous  $\text{TiO}_2$ -0.69H. Reprinted with permission from Ma *et al.*, ACS Catal. 8(10), 9711–9721 (2018). Copyright 2018 American Chemical Society.

phous  $\text{TiO}_2$ , where the characteristic H chemical shift  $\delta$  value in  $^1\text{H}$  nuclear magnetic resonance spectroscopy has a negative peak ( $-0.6$  ppm) and this peak of  $\delta$  grows with the increase in the hydrogenation time.<sup>57</sup>

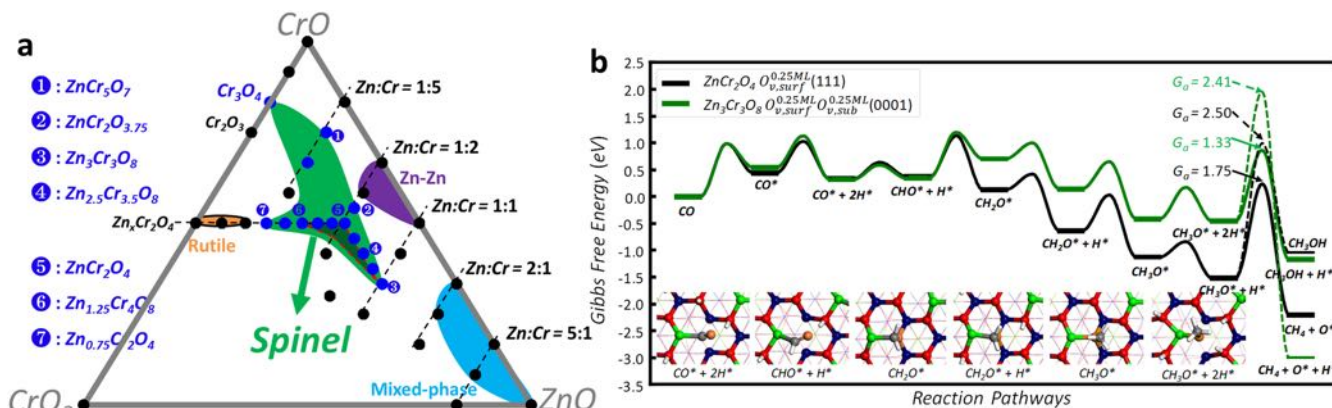


**FIG. 6.** (a) Ternary Zn-Cr-O phase diagram. The blue circles labeled by numbers indicate the chemical composition and the green region in the middle of the map are the compositions that have the spinel-type skeleton structure as the global minimum. (b) Gibbs free energy reaction profiles for syngas conversion on two ZnCrO catalysts at 573 K and 2.5 MPa syngas ( $\text{H}_2:\text{CO} = 1.5$ ). The reaction snapshots are shown in the inset of (b), where the color scheme for atoms is as follows: Zn: green; Cr: purple; O: red; O in CO: orange; C: gray, and H: white. Reprinted with permission from S. Ma, S.-D. Huang, and Z.-P. Liu, "Dynamic coordination of cations and catalytic selectivity on zinc-chromium oxide alloys during syngas conversion," Nat. Catal. (published online 2019). Copyright 2019 Nature Publishing Group.

### C. Syngas conversion on ZnCrO catalysts with varied Zn:Cr ratio

Zinc-chromium oxide (ZnCrO) catalyst is the first generation industry catalysts for syngas-to-methanol. Experiment shows that the catalytic activity is significantly affected by Zn:Cr ratios:<sup>58–62</sup> the best activity and selectivity are achieved at Zn:Cr =  $\sim 1:1$ , while the Zn:Cr = 1:2 catalysts yield rather poor activity.<sup>62</sup> The atomic structure of ZnCrO catalysts with Zn:Cr = 1:1 remains, however, uncertain as no clear evidence of ZnO formation was found, although the X-ray diffraction (XRD) patterns exhibit peak broadening and small peak shifting with respect to the 1:2 phase,  $\text{ZnCr}_2\text{O}_4$  spinel phase.<sup>62–64</sup> The structural uncertainty in the ZnCrO catalyst is, in fact, quite typical for multicomponent oxide catalysts, where the atomic structures of the active sites are often unknown.

To resolve where and how syngas conversion occurs on the ZnCrO catalyst, we have performed the SSW-NN simulation to obtain the ZnCrO global dataset and to build a robust and accurate ZnCrO G-NN potential. Our simulations contain structures from 10 to 84 atoms per cell and cover different Zn:Cr:O ratios, i.e.,  $\text{ZnO}$ ,  $\text{CrO}_x$ ,  $\text{ZnCr}_x\text{O}_y$ , with different morphology forms, e.g., bulk, layers, and clusters. The final ZnCrO global dataset contains 38 285 structures. The ZnCrO G-NN potential contains 324 PTSDs for each element, i.e., 132 two-body PTSDs, 170 three-body PTSDs, and 22 four-body PTSDs, and compatibly, the network involves three-hidden layers (324–80–60–60–1 net), equivalent to 103 743 network parameters in total. The final RMSEs of energy and force are 4.3 meV/atom and 0.128 eV/Å, respectively.<sup>65</sup>

Based on the ZnCrO G-NN potential, the global PES of ZnCrO is explored and the thermodynamics phase diagram of Zn-Cr-O is constructed. It reveals a small stable composition island, i.e., Zn:Cr:O = 6:6:16–3:8:16, where the oxide alloy crystallizes into a spinel phase [Fig. 6(a)]. At Zn:Cr = 1:1, a  $\text{Zn}_3\text{Cr}_3\text{O}_8$  metastable crystal phase is present, also with the spinel crystal structure, but contains the highest concentration of unusual  $[\text{ZnO}_6]$  octahedra ( $\text{O}_h$ ) in the bulk compared to the other spinel crystals. This subtle structural difference turns out to be critical to affect the syngas conversion

activity and selectivity profoundly. Further DFT investigation on the syngas conversion reaction on  $\text{Zn}_3\text{Cr}_3\text{O}_8$  and  $\text{ZnCr}_2\text{O}_4$  proves that the  $\text{Zn}_3\text{Cr}_3\text{O}_8$  surface can generate the four-coordinated planar  $\text{Cr}^{2+}$  cation in site that is critical for methanol selectivity. On the other hand, the  $\text{ZnCr}_2\text{O}_4$  phase shows a low catalytic activity and leads to methane dominantly [Fig. 6(b)].

The microkinetics simulation based on DFT reaction energetics (methanol yield:  $\sim 670 \text{ g kg}_{\text{cat}}^{-1} \text{ h}^{-1}$  on  $\text{Zn}_3\text{Cr}_3\text{O}_8$ ; methane yield:  $\sim 0.08 \text{ g kg}_{\text{cat}}^{-1} \text{ h}^{-1}$  on  $\text{ZnCr}_2\text{O}_4$ ) further rationalizes the sharp difference in activity and selectivity observed in experiment: the  $\text{ZnCrO}$  catalysts with  $\text{Zn}:\text{Cr} = 1:1$  shows high activity and high methanol selectivity (methanol yield  $80\text{--}600 \text{ g}^* \text{ kg}_{\text{cat}}^{-1} \text{ h}^{-1}$  and selectivity 80% at 573 K), but the  $\text{ZnCrO}$  catalysts with  $\text{Zn}:\text{Cr} = 1:2$  shows low activity and low methanol selectivity [ $< 5 \text{ g}^* \text{ kg}_{\text{cat}}^{-1} \text{ h}^{-1}$  with 14% selectivity to methanol at 573 K and  $\sim 82\%$  to hydrocarbon (91%  $\text{CH}_4$ ) at 673 K].<sup>62,66</sup> The findings on  $\text{ZnCrO}$  catalysts not only strengthen our understandings, from bulk to surfaces and to active sites, on the high-temperature syngas conversion on oxides but also suggest other complex oxide systems hotly debated in experiment, e.g.,  $\text{ZnZrO}$ ,  $\text{CuZnO}$ ,  $\text{ZnMnO}$ , and  $\text{ZnFeO}$ ,<sup>66–68</sup> should now be possible to explore with the advent of the SSW-NN method.

#### IV. REMARKS AND PROSPECTS

This perspective overviews the SSW-NN method and its recent applications in heterogeneous catalysis. While SSW-NN holds great promise in solving some challenging tasks in heterogeneous catalysis, ranging from catalyst active site structure to catalytic activity as demonstrated in the above examples, one must bear in mind that a successful application of the SSW-NN method relies much on the sampled dataset to the target problem. The SSW sampling becomes frustrated for some molecular reactions and for systems with too large degrees of freedom, as elaborated below.

- (i) Reaction sampling for molecular reactions have a high computational cost even with the SSW method. It is especially problematic for reactions with a sharp TS region (i.e., characterized by a large negative curvature), where the exact TS position is difficult to capture by random sampling. As introduced above, the current NN potential generally focuses on materials such as  $\text{TiO}_2$  and  $\text{ZnCrO}$ , and a giant step forward would couple molecular reactions with the solid materials to establish reactive NN potentials for heterogeneous catalysis.
- (ii) The iterative self-learning in building the global NN potential may become highly computational when the system size is large and the bonding complexity increases. In particular, the large configurational space of bonding environment in multielement systems is a key problem in constructing G-NN. For example, there are many possible bonding patterns for carbon with other elements (C, H, O, and N) in organic chemistry, which leads to great difficulty in building a general-purpose reactive NN potential for organic chemistry.

To enhance the reaction sampling and to reduce the system degree of freedom effectively, we expect that the combination of other techniques with SSW-NN, such as pattern recognition artificial intelligence methods, coarse graining, and rigid body methods

could be the future direction to power up SSW-NN for complex catalysis problems. Our ongoing implementation of LASP software<sup>27</sup> could help us to fulfill this goal by integrating different techniques in one platform, which aims to accelerate the material simulation in the future.

#### ACKNOWLEDGMENTS

This work was supported by the National Key Research and Development Program of China (Grant No. 2018YFA0208600) and National Science Foundation of China (Grant Nos. 21573149, 21533001, and 91745201).

The authors declare no competing financial interests.

#### REFERENCES

- <sup>1</sup>I. E. Wachs and C. A. Roberts, *Chem. Soc. Rev.* **39**(12), 5002–5017 (2010).
- <sup>2</sup>J. K. Nørskov, T. Bligaard, B. Hvolbæk, F. Abild-Pedersen, I. Chorkendorff, and C. H. Christensen, *Chem. Soc. Rev.* **37**(10), 2163–2171 (2008).
- <sup>3</sup>T. F. Jaramillo, K. P. Jørgensen, J. Bonde, J. H. Nielsen, S. Horch, and I. Chorkendorff, *Science* **317**(5834), 100–102 (2007).
- <sup>4</sup>U. Deka, I. Lezcano-Gonzalez, B. M. Weckhuysen, and A. M. Beale, *ACS Catal.* **3**(3), 413–427 (2013).
- <sup>5</sup>R. G. Parr, *Horizons of Quantum Chemistry* (Springer, 1980), pp. 5–15.
- <sup>6</sup>A. Y. Khodakov, W. Chu, and P. Fongarland, *Chem. Rev.* **107**(5), 1692–1744 (2007).
- <sup>7</sup>S. K. Seth, I. Saha, C. Estarellas, A. Frontera, T. Kar, and S. Mukhopadhyay, *Cryst. Growth Des.* **11**(7), 3250–3265 (2011).
- <sup>8</sup>J. Kotakoski, A. Krasheninnikov, U. Kaiser, and J. Meyer, *Phys. Rev. Lett.* **106**(10), 105505 (2011).
- <sup>9</sup>T. Kohonen, *Neural Networks* **1**(1), 3–16 (1988).
- <sup>10</sup>J. P. Perdew, K. Burke, and M. Ernzerhof, *Phys. Rev. Lett.* **77**(18), 3865–3868 (1996).
- <sup>11</sup>J. Heyd, G. E. Scuseria, and M. Ernzerhof, *J. Chem. Phys.* **118**(18), 8207–8215 (2003).
- <sup>12</sup>B. G. Sumpter and D. W. Noid, *Chem. Phys. Lett.* **192**(5–6), 455–462 (1992).
- <sup>13</sup>T. H. Fischer, W. P. Petersen, and H. P. Lüthi, *J. Comput. Chem.* **16**(8), 923–936 (1995).
- <sup>14</sup>L. Raff, M. Malshe, M. Hagan, D. Doughan, M. Rockley, and R. Komanduri, *J. Chem. Phys.* **122**(8), 084104 (2005).
- <sup>15</sup>S. Manzhos, X. Wang, R. Dawes, and T. Carrington, *J. Phys. Chem. A* **110**(16), 5295–5304 (2006).
- <sup>16</sup>J. R. Boes and J. R. Kitchin, *Mol. Simul.* **43**(5–6), 346–354 (2017).
- <sup>17</sup>G. Sun and P. Sautet, *J. Am. Chem. Soc.* **140**(8), 2812–2820 (2018).
- <sup>18</sup>N. Artrith and A. M. Kolpak, *Nano Lett.* **14**(5), 2670–2676 (2014).
- <sup>19</sup>N. Artrith and A. M. Kolpak, *Comput. Mater. Sci.* **110**, 20–28 (2015).
- <sup>20</sup>J. S. Elias, N. Artrith, M. Bugnet, L. Giordano, G. A. Botton, A. M. Kolpak, and Y. Shao-Horn, *ACS Catal.* **6**(3), 1675–1679 (2016).
- <sup>21</sup>N. Artrith, B. Hiller, and J. Behler, *Phys. Status Solidi B* **250**(6), 1191–1203 (2013).
- <sup>22</sup>S. Kirkpatrick, C. D. Gelatt, and M. P. Vecchi, *Science* **220**(4598), 671–680 (1983).
- <sup>23</sup>S. Sivanandam, and S. Deepa, *Introduction to Genetic Algorithms* (Springer, 2008), pp. 165–209.
- <sup>24</sup>D. J. Wales and J. P. Doye, *J. Phys. Chem. A* **101**(28), 5111–5116 (1997).
- <sup>25</sup>C. Shang and Z.-P. Liu, *J. Chem. Theory Comput.* **9**(3), 1838–1845 (2013).
- <sup>26</sup>X.-J. Zhang, C. Shang, and Z.-P. Liu, *J. Chem. Theory Comput.* **9**(7), 3252–3260 (2013).
- <sup>27</sup>S. D. Huang, C. Shang, P. L. Kang, X. J. Zhang, and Z. P. Liu, “LASP: Fast global potential energy surface exploration,” *Wiley Interdiscip. Rev.: Comput. Mol. Sci.* (published online 2019).
- <sup>28</sup>C. Shang, X.-J. Zhang, and Z.-P. Liu, *Phys. Chem. Chem. Phys.* **16**(33), 17845–17856 (2014).



- <sup>29</sup>W. S. McCulloch and W. Pitts, *Bull. Math. Biophys.* **5**(4), 115–133 (1943).
- <sup>30</sup>J. Behler and M. Parrinello, *Phys. Rev. Lett.* **98**(14), 146401 (2007).
- <sup>31</sup>J. Behler, *J. Chem. Phys.* **134**(7), 074106 (2011).
- <sup>32</sup>J. Behler, *J. Phys.: Condens. Matter* **26**(18), 183001–1830024 (2014).
- <sup>33</sup>A. P. Bartók, R. Kondor, and G. Csányi, *Phys. Rev. B* **87**(18), 184115 (2013).
- <sup>34</sup>K. Schütt, H. Glawe, F. Brockherde, A. Sanna, K. Müller, and E. Gross, *Phys. Rev. B* **89**(20), 205118 (2014).
- <sup>35</sup>J. Behler, *J. Chem. Phys.* **145**(17), 170901 (2016).
- <sup>36</sup>S.-D. Huang, C. Shang, X.-J. Zhang, and Z.-P. Liu, *Chem. Sci.* **8**(9), 6327–6337 (2017).
- <sup>37</sup>S.-D. Huang, C. Shang, P.-L. Kang, and Z.-P. Liu, *Chem. Sci.* **9**(46), 8644–8655 (2018).
- <sup>38</sup>J. Behler, *Phys. Chem. Chem. Phys.* **13**(40), 17930–17955 (2011).
- <sup>39</sup>J. Behler, *Angew. Chem., Int. Ed.* **56**(42), 12828–12840 (2017).
- <sup>40</sup>D. Coyle, G. Prasad, and T. M. McGinnity, *IEEE Trans. Syst. Man Cybern. B* **39**(6), 1458–1471 (2009).
- <sup>41</sup>T. Domhan, J. T. Springenberg, and F. Hutter, in *IJCAI*, 2015.
- <sup>42</sup>S.-h. Guan, C. Shang, S.-D. Huang, and Z.-P. Liu, *J. Phys. Chem. C* **122**(50), 29009–29016 (2018).
- <sup>43</sup>S. Ma, S.-D. Huang, Y.-H. Fang, and Z.-P. Liu, *ACS Appl. Energy Mater.* **1**(1), 22–26 (2018).
- <sup>44</sup>S. Ma, S.-D. Huang, Y.-H. Fang, and Z.-P. Liu, *ACS Catal.* **8**(10), 9711–9721 (2018).
- <sup>45</sup>X.-J. Zhang, C. Shang, and Z.-P. Liu, *Phys. Chem. Chem. Phys.* **19**(6), 4725–4733 (2017).
- <sup>46</sup>S.-H. Choe, C.-J. Yu, K.-C. Ri, J.-S. Kim, U.-G. Jong, Y.-H. Kye, and S.-N. Hong, *Phys. Chem. Chem. Phys.* **123**(15), 9735–9744 (2019).
- <sup>47</sup>X. Chen, L. Liu, and F. Huang, *Chem. Soc. Rev.* **44**(7), 1861–1885 (2015).
- <sup>48</sup>X. Chen, L. Liu, Y. Y. Peter, and S. S. Mao, *Science* **331**(6018), 746–750 (2011).
- <sup>49</sup>A. Naldoni, M. Allieta, S. Santangelo, M. Marelli, F. Fabbri, S. Cappelli, C. L. Bianchi, R. Psaro, and V. Dal Santo, *J. Am. Chem. Soc.* **134**(18), 7600–7603 (2012).
- <sup>50</sup>X. Yu, B. Kim, and Y. K. Kim, *ACS Catal.* **3**(11), 2479–2486 (2013).
- <sup>51</sup>N. Liu, C. Schneider, D. Freitag, M. Hartmann, U. Venkatesan, J. Müller, E. Spiecker, and P. Schmuki, *Nano Lett.* **14**(6), 3309–3313 (2014).
- <sup>52</sup>H. Lu, B. Zhao, R. Pan, J. Yao, J. Qiu, L. Luo, and Y. Liu, *RSC Adv.* **4**(3), 1128–1132 (2014).
- <sup>53</sup>Y. H. Hu, *Angew. Chem., Int. Ed.* **51**(50), 12410–12412 (2012).
- <sup>54</sup>X. Chen, L. Liu, Z. Liu, M. A. Marcus, W.-C. Wang, N. A. Oyler, M. E. Grass, B. Mao, P.-A. Glans, and Y. Y. Peter, *Sci. Rep.* **3**, 1510 (2013).
- <sup>55</sup>Z. Wang, C. Yang, T. Lin, H. Yin, P. Chen, D. Wan, F. Xu, F. Huang, J. Lin, and X. Xie, *Energy Environ. Sci.* **6**(10), 3007–3014 (2013).
- <sup>56</sup>U. Aschauer and A. Selloni, *Phys. Chem. Chem. Phys.* **14**(48), 16595–16602 (2012).
- <sup>57</sup>Y. Guo, S. Chen, Y. Yu, H. Tian, Y.-L. Zhao, J.-C. Ren, C. Huang, H. Bian, M. Huang, and L. An, *J. Am. Chem. Soc.* **141**(21), 8407–8411 (2019).
- <sup>58</sup>K. Waugh, *Catal. Today* **15**(1), 51–75 (1992).
- <sup>59</sup>M. C. Molstad and B. F. Dodge, *Ind. Eng. Chem.* **27**(2), 134–140 (1935).
- <sup>60</sup>E. Errani, F. Trifiro, A. Vaccari, M. Richter, and G. Del Piero, *Catal. Lett.* **3**(1), 65–72 (1989).
- <sup>61</sup>M. C. Bradford, M. V. Konduru, and D. X. Fuentes, *Fuel Process. Technol.* **83**(1–3), 11–25 (2003).
- <sup>62</sup>H. Song, D. Laudenschleger, J. J. Carey, H. Ruland, M. Nolan, and M. Muhler, *ACS Catal.* **7**(11), 7610–7622 (2017).
- <sup>63</sup>G. Del Piero, F. Trifiro, and A. Vaccari, *J. Chem. Soc., Chem. Commun.* **1984**(10), 656–658.
- <sup>64</sup>M. Bertoldi, B. Fubini, E. Giamello, F. Trifirò, and A. Vaccari, *J. Chem. Soc., Faraday Trans.* **84**(5), 1405–1421 (1988).
- <sup>65</sup>S. Ma, S.-D. Huang, and Z.-P. Liu, “Dynamic coordination of cations and catalytic selectivity on zinc-chromium oxide alloys during syngas conversion,” *Nat. Catal.* (published online 2019).
- <sup>66</sup>K. Cheng, B. Gu, X. Liu, J. Kang, Q. Zhang, and Y. Wang, *Angew. Chem., Int. Ed.* **128**(15), 4803–4806 (2016).
- <sup>67</sup>M. Behrens, F. Studt, I. Kasatkin, S. Kühn, M. Hävecker, F. Abild-Pedersen, S. Zander, F. Girgsdies, P. Kurr, and B.-L. Kniep, *Science* **336**, 893–897 (2012).
- <sup>68</sup>J. Wang, G. Li, Z. Li, C. Tang, Z. Feng, H. An, H. Liu, T. Liu, and C. Li, *Sci. Adv.* **3**(10), e1701290 (2017).